Numerical and experimental study of the flow around a 4:1 rectangular cylinder at moderate Reynolds number

Amandine Guissart*, Thomas Andrianne, Greg Dimitriadis, Vincent E. Terrapon

Department of Aerospace and Mechanical Engineering, University of Liège, Allée de la Découverte 9, 4000 Liège, Belgium

Abstract

This paper presents the results of investigations into the flow around a rectangular cylinder with a chord-to-depth ratio equal to 4. The studies are performed through wind tunnel dynamic pressure measurements along a cross-section combined with Unsteady Reynolds-Averaged Navier-Stokes (URANS) and Delayed-Detached Eddy Simulation (DDES). These experimental and numerical studies are complementary and combining them allows a better understanding of the unsteady dynamics of the flow. The comparison of experimental and numerical data is performed using statistics and Dynamic Mode Decomposition. It is shown that the rectangular cylinder involves complex separation-reattachment phenomena that are highly sensitive to the Reynolds number. In particular, the mean lift slope $\overline{c}_{l_\alpha}$ increases rapidly with the Reynolds number in the range $7.8\times10^3 \leq \mathrm{Re} \leq 1.9\times10^4$ due to the modification of the mean vortex strength, thickness and distance from the surface. Additionally, it is shown that both URANS and DDES simulations fail to accurately predict the flow at all the different incidence angles considered. The URANS approach is able to qualitatively estimate the spatio-temporal variations of vortices for incidences below the stall angle $\alpha = 4°$. Nonetheless, URANS does not predict stall, while DDES correctly identifies the stall angle observed experimentally.

Keywords: bluff body, rectangular cylinder, URANS, DDES, unsteady pressure measurements, aerodynamics.

1. Introduction

Despite the simple two-dimensional geometries involved, the flow around bodies of elongated rectangular cross section are highly complex because of the three-dimensional nature of turbulence and the unsteady separation and reattachment dynamics characterizing bluff bodies. Rectangular cylinders at zero incidence have been extensively studied, first experimentally (e.g. Nakaguchi et al., 1968; Nakamura and Mizota, 1975; Washizu et al., 1978; Okajima, 1983; Stokes and Welsh, 1986) and then numerically (e.g. Tamura et al., 1993; Yu and Kareem, 1998; Shimada and Ishihara, 2002). These authors have shown that the flow dynamics around such cross sections is mainly influenced by the ratio of the chord c to the deph d of the cross section. In particular, Shimada and Ishihara (2002) investigated the impact of the c/d ratio at zero incidence through Unsteady Reynolds-Average Navier-Stokes (URANS) simulations at $\mathrm{Re} = 2.2\times10^4$, this Reynolds number being defined as $\mathrm{Re} = U_\infty d/\nu$, where U_∞ and ν are the freestream velocity and the kinematic viscosity, repectively. Shimada and Ishihara (2002) divided the aerodynamic behavior into three main categories based on the dynamics of the shear layer. For short cylinders with $c/d \leq 2.8$, flow separation occurs at the leading edges and the rectangular cross section is too short to allow shear layer reattachment. The flow is thus fully separated and vortices are periodically shed from the leading edges of the cylinder. On rectangular cross sections with a ratio $2.8 < c/d < 6$, the shear layer reattaches periodically and vortex shedding occurs from both the leading and trailing edges. Finally, for longer rectangular cylinders with $c/d \geq 6$, the flow is able to fully reattach and vortices are shed from the trailing edges.

In this context, the Benchmark on the Aerodynamics of a Rectangular Cylinder (BARC) (Bartoli et al., 2008) provides experimental and numerical contributions to the study of a 5:1 rectangular cylinder. Bruno et al. (2014) compared more than 70 studies in terms of bulk parameters, flow and pressure statistics, as well as spanwise correlations. Among the principal conclusions, Bruno et al. (2014) reported a narrow distribution of results obtained for the Strouhal number and the mean drag coefficient while those collected for the standard deviation of the lift coefficient are significantly dispersed. It was argued that this scattering is caused by the high sensitivity of the flow along the upper and lower surfaces of the rectangular cylinder to small differences in the wind tunnel setup and in the simulation parameters. Within the framework of the BARC, Schewe (2013) investigated experimentally the impact of Reynolds number in the range between 4×10^3 and 4×10^5 on the aerodynamic coefficients. He showed that the Reynolds number has a minor influence on both the drag coefficient and the Strouhal number, but significantly impacts the lift coefficient and particularly the lift curve slope. Schewe (2013) argued that an increase in the Reynolds number could correspond to an increase in the turbulence level which would cause a shift downstream of the mean reattachment point on the lower surface (for a cylinder at positive angle of attack). This would lead to a modification of the

*Corresponding author
Email address: aguissart@alumni.uliege.be (Amandine Guissart)

flow topology that could impact the pressure coefficient distribution and therefore the lift. The need for the wind engineering community to capture accurately the slope of the lift coefficient is obvious: it appears (i) in the calculation of the critical wind speed in the quasi-steady theory of galloping and (ii) in the calculation of the buffeting response of structures subject to turbulent wind flows. More recently, Patruno et al. (2016) performed URANS and Large Eddy Simulations (LES) at three angles of attack. They reported large discrepancies between URANS and LES results for the different incidences. Moreover, they showed that URANS is not able to correctly estimate the internal organization of the recirculation bubble, which impacts the estimation of the spatio-temporal pressure coefficient and subsequently the load coefficients. Finally, Mannini et al. (2017) used pressure and load measurements to investigate the effects of the incidence, Reynolds number and turbulent intensity on the flow and the subsequent bulk parameters. In particular, the Reynolds-number dependence of force coefficients and the effect of the incoming turbulence on the vortex-shedding mechanism were highlighted.

As an extension of the studies performed by Patruno et al. (2016) and Mannini et al. (2017), the present work investigates both experimentally and numerically the flow around a rectangular cylinder of aspect ratio $^{c}/_{d} = 4$, i.e., slightly shorter that in the context of the BARC but exhibiting similar dynamics. The spatio-temporal pressure distribution along a cross section of the cylinder is acquired by carrying out unsteady pressure measurements at different incidences and for $7.8 \times 10^3 < \mathrm{Re} < 1.9 \times 10^4$. The flow is also investigated through Computational Fluid Dynamics (CFD) using both URANS and Delayed-Detached Eddy Simulation (DDES) approaches. The objective of the present study is two-fold: i) to determine the effects of the rectangle incidence and freestream velocity on the variation of the flow topology and the aerodynamic loads, and ii) to assess the capability of URANS and DDES to provide a sufficiently accurate estimation of the flow and the subsequent aerodynamic loads for different incidences.

2. Methodology

Sections 2.1 and 2.2 are dedicated to the description of the experiments and the setup of the CFD simulations, respectively. An extensive description of the experimental set-up can be found in Guissart (2017).

2.1. Experimental approach

The measurements are conducted in a Göttingen-type wind tunnel whose freestream turbulence intensity is below 2%. The test section is 5 m long, 2.5 m wide and 1.8 m high. The main Reynolds number studied in the following is $\mathrm{Re} = 1.1 \times 10^4$, which is based on a freestream velocity $U_\infty = 8.3\,\mathrm{m/s}$. Four additional freestream velocities are also considered to study the impact of the Reynolds number in the range between 7.8×10^3 and 1.9×10^4. These velocities are $U_\infty = 6\,\mathrm{m/s}$, $10.6\,\mathrm{m/s}$, $12.8\,\mathrm{m/s}$ and $15\,\mathrm{m/s}$.

The model consists of a hollow rectangular aluminum tube of 2 mm thickness and 1 m length. Its cross-section is 8 cm × 2 cm, which corresponds to a chord-to-depth ratio $^{c}/_{d} = 4$. The cross-section edges are not perfectly sharp and their radius r_c is such that $^{r_c}/_{d} = 1.5\%$. The tube is attached horizontally on one of its sides with ball bearings on a vertical beam. This assembly leads to a single degree of freedom in pitch that is clamped once the desired incidence is imposed. The other side of the tube is located at a distance of $0.4c$ from the wind tunnel wall to reduce three-dimensional effects. A wooden plate of dimensions $15.6c \times 17.8c$ is added next to the vertical beam to reduce as much as possible the impact of the mounting on the flow around the rectangular cylinder. As depicted in Fig. 1, the rectangular tube is located relatively far from the edges of the wooden plate and the boundary effects are thus assumed to be small.

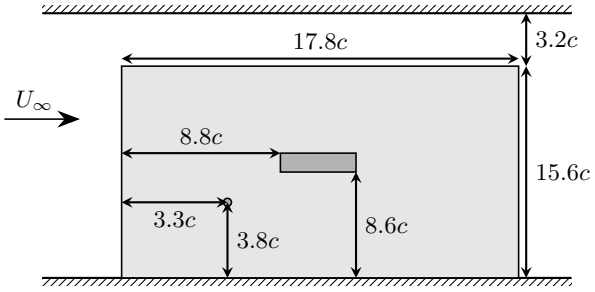

Figure 1: Schematic side view of the mounting apparatus where the rectangular cylinder is depicted in dark gray, the wooden plate in light gray, and the small disk represents the point where the reference freestream velocity and static pressure are measured.

The pressure is sampled at several pressure taps located on a cross-section of the rectangular cylinder as depicted in Fig. 2. This section located at the mid-span of the cylinder is covered with 36 taps separated by a nominal distance of 5 mm or 6.25% of the chord. Note that after the pressure taps were drilled manually, their exact location is measured to an accuracy of 0.2 mm. In the following, the taps are identified by their non-dimensional curvilinear abscissa $\bar{r} = {}^{r}/_{c}$, r being defined in Fig. 2. Pressure is measured with a multi-channel DYNAMIC PRESSURE MEASUREMENT SYSTEM made by TFI and working in the range ±10 hPa to ±35 hPa. This transducer measures $p - p_\infty$, the difference between the pressure p at a tap and a reference pressure p_∞ measured at the reference point shown in Fig. 1. The pressure taps are connected to the pressure transducer by TRANS CONTINENTAL MANUFACTURING tubes that are 1.34 m long and have a documented internal diameter of 1.32 mm. Each tube forms a pneumatic line that acts as a filter and causes amplitude and phase distortions of the unsteady pressure signal to be measured. Therefore, a correction is applied as a post-processing step to retrieve the local unsteady pressure at each tap. In particular, the theoretical correction proposed by Bergh and Tijdeman (1965) is chosen. The freestream velocity and static pressure being known, the pressure coefficient $C_p = \frac{p - p_\infty}{{}^{1}/_{2}\rho_\infty U_\infty}$ at each tap location can then be straightforwardly computed. The pressure distribution is acquired for angles of attack ranging from $-7°$ to $8°$, the incidence angle being set with an accuracy of $0.2°$. The sampling frequency f_s is set to 500 Hz and each set of experiments lasts for 60 s. Assuming

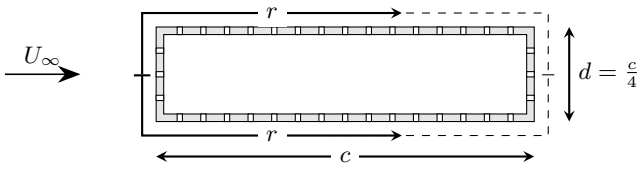

Figure 2: Schematic sectional view of the pressure taps located on the rectangular cylinder and definition of the coordinate r along the cylinder cross-section surface.

the Strouhal number $\mathrm{St} = {}^{fd}/_{U_\infty} = 0.13$ (Washizu et al., 1978) where f is the shedding frequency of the rectangular cylinder, this sampling frequency corresponds to at least $5f$ and each set contains more than 2 000 shedding cycles.

The pressure coefficient is first computed from the raw data and filtered using a Butterworth 12^{th} order band-pass filter with a frequency band from 10 to 200 Hz. Then, the amplitude and phase distortions caused by the tube lines on the time response of C_p are corrected by applying the method proposed by Bergh and Tijdeman (1965). Note that the sensitivity of the corrected pressure to the input parameters required by this method has been studied, and it has been demonstrated that the conclusions exposed below are robust to uncertainties associated with them (Guissart, 2017). Aerodynamic loads applied on the rectangle are calculated by integrating the C_p distribution along the rectangle surfaces. The integration is performed using the trapezoidal rule. This leads to the two-dimensional sectional coefficients of lift c_l, drag c_d and pitching moment c_m, the latter being computed about the cross section center and defined positive nose-up. These three load coefficients are computed based on the chord length c. Finally, the Strouhal number is computed through Fourier analysis performed on the lift coefficient.

2.2. *Computational approaches*

Two CFD simulation tools are used to compute the flow and aerodynamic loads on the 4:1 cylinder: URANS and DDES. The simulations are performed in OpenFOAM®. The implementation characteristics of each model are presented below.

2.2.1. URANS *simulations*

The chosen URANS model is the $k-\omega$ SST proposed by Menter and Esch (2001) and modified by Menter et al. (2003). A transient solver for incompressible flow based on the PIMPLE algorithm is used with a non-dimensional time step ${}^{\Delta t U_\infty}/_{c}$ set to 10^{-3}, i.e., ${}^{1}/_{1700}{}^{\text{th}}$ of a typical shedding cycle. The second order implicit backward Euler scheme is used to advance the equations in time and second order schemes are chosen for spatial discretization. In particular, the velocity gradient $\partial_i u_j$ is discretized through a second order, upwind-biased scheme.

As depicted in Fig. 3, the computational domain is a square of dimensions $50c \times 50c$ centered vertically on the centroid of the rectangular cylinder. The upstream and downstream borders of this square are respectively distant of $19.5c$ and $30.5c$ from the rectangle center. These dimensions are similar to those used in most of the numerical studies performed in the context of the BARC (Bruno et al., 2014). The mesh is divided into an unstructured and a structured parts. The structured region consists of a disc of radius $15d$ centered on the rectangle and the zone of the wake located downstream of the body. The simulations are wall-resolved and the first mesh point away from the surface is set such that $y^+ \approx 0.7$ for most of the cells around the rectangle. The grid consists of 140 cells spread along the chord of the rectangular cylinder, 130 along its depth, 100 cells along the radius of the circle surrounding the rectangle and 90 cells discretizing horizontally the wake. It contains 75 000 hexahedra and the grid independence of the results was verified through a mesh convergence study.

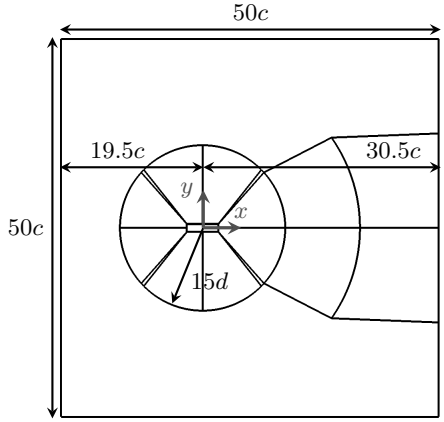

Figure 3: Computational domain used for the URANS and DDES simulations.

At walls, the no-slip boundary condition is imposed for the velocity and a zero-gradient condition is set for the pressure. Dirichlet conditions are imposed for the turbulent scalars using the automatic near-wall treatment proposed by Menter and Esch (2001). At the inlet, the freestream velocity is imposed and the pressure gradient is set to zero. The value of the turbulent kinetic energy k_∞ is based on an inlet freestream turbulence intensity of 0.3% and the specific dissipation rate ω_∞ is such that the turbulent eddy viscosity verifies $\nu_t = 5 \times 10^{-3} \nu$ (Menter and Esch, 2001). The outlet corresponds to a zero-gradient for the velocity and turbulent scalars, while the pressure is enforced. Finally, a slip boundary condition is imposed for all variables at the upper and lower boundaries of the domain, allowing only a streamwise variation.

2.2.2. DDES *simulations*

The DDES simulations carried out within the context of the present work are based on the original formulation of the Spalart-Allmaras model (Spalart et al., 1997). The setup is very similar to that of URANS, except for a few particular points specific to DDES.

As for URANS simulations, the transient incompressible solver PIMPLE is selected. For stability purposes, the non-dimensional time-step is decreased compared to the URANS cases and set to 6.25×10^{-4}. Similarly to the URANS setup, a backward Euler scheme is chosen for temporal discretization. The same second-order schemes are also used for spatial discretization, except for the non-linear advective term, which is discretized with a Linear Upwind Stabilized Transport (LUST) scheme, as suggested by Patruno et al. (2016).

The two-dimensional computational domain depicted in Fig. 3 is extruded along the z-direction to obtain a spanwise length $s = c$. This dimension has been used in LES studies performed on similar cases (e.g. Yu and Kareem, 1998; Bruno et al., 2010) and verifies the criterion $s/c \geq 1$ suggested by Tamura et al. (1998). Note however that Mannini et al. (2011) showed that this common choice for the span is not enough to allow the free development of large-scale turbulent structures, which could lead to an overestimation of the load coefficients' second order statistics. Spalart and Streett (2001) argued that the geometry-dependent turbulence structures are generated in the "focus region" and that the maximum grid spacing Δ_0 within that region is the principal measure of the spatial resolution in DDES. This region is assumed here to extend up to half a chord downstream of the rectangular cylinder's trailing edges and the DDES mesh is designed to obtain $\Delta_0 = c/64$, similarly to Mannini et al. (2011) who demonstrated the strong impact of this parameter on the results. The spanwise discretization is $\Delta z = c/64$ and the grid in the $x-y$ plane has to be modified compared to URANS grid to keep the extent of the "focus region". In particular, the chord and the depth of the rectangular cylinder are divided into 200 and 130 cells, respectively, while 110 cells are spread into the wake. Finally, a mesh made of 8.2 M cells is obtained.

The boundary conditions for pressure and velocity are the same as the ones described for URANS. As a smooth freestream flow is assumed, a Dirichlet boundary condition $\tilde{\nu} = 0$ is imposed at the inlet while a Neumann condition is set for the outlet. A slip condition is imposed on the upper and lower boundaries. Finally, periodic boundary conditions are adopted on the two boundaries normal to the extrusion direction.

The DDES results presented below are based on a computed time window containing 150 non-dimensional time instances, i.e., roughly 80 shedding cycles. A convergence study showed that the mean and standard deviation of the aerodynamic coefficients converged to within 5% after 150 time instances. Moreover, the first 100 of the total 250 non-dimensional time units contained in each DDES simulation were discarded in order to eliminate the transient response.

2.3. Comparison of the different approaches

The experimental (EXP) and numerical results are compared through usual statistical analysis and via a spatio-temporal decomposition technique (Dynamic Mode Decomposition, or DMD).

First and second order statistics are computed on the time response of the pressure and aerodynamic load coefficients. The time-averaged values and the corresponding standard deviations are respectively denoted by $\bar{\cdot}$ and $\cdot'$. The pressure distribution of interest corresponds to C_p along the cross-section of the rectangular cylinder. The three-dimensional pressure distributions calculated by the DDES simulations are first averaged along the z-direction. Note that the second order statistics resulting from this averaging step are small, which is probably due to the short span length that does not allow the development of large-scale structures (Mannini et al., 2011). First and second order statistics are then computed on the resulting $\langle C_p{}^{\text{DDES}}(\mathbf{x}, t)\rangle_z$. Finally, because EXP and URANS results are two-dimensional, the corresponding statistics are computed without this span-averaging step.

The spatio-temporal EXP and CFD results are compared using DMD, a technique proposed by Schmid (2010) that decomposes data into single frequency modes $\boldsymbol{\phi}_k^{\text{DMD}}$ describing the dynamic process. The dynamical flow features are extracted from a temporal sequence of N snapshots $\mathbf{v}_n$ equidistant in time, each snapshot being a column vector of M two or three-dimensional spatial data. In particular, the $M \times N$ matrix of snapshots $\mathbf{V}_1^N = \{\mathbf{v}_1, \mathbf{v}_2, \ldots, \mathbf{v}_N\}$ is decomposed into the variable-separated finite sum

$$\mathbf{V}_1^N(\mathbf{x}, t) = \sum_{k=1}^{K} q_k^{\text{DMD}} \boldsymbol{\phi}_k^{\text{DMD}} \exp\left(\lambda_k^{\text{DMD}} \mathbf{t}\right), \tag{1}$$

where, $\boldsymbol{\phi}_k^{\text{DMD}}$ is the k^{th} spatial mode. The time response is expressed as $q_k^{\text{DMD}} \exp\left(\lambda_k^{\text{DMD}} \mathbf{t}\right)$, where q^{DMD} and λ_k^{DMD} are respectively the complex amplitude and frequency associated with the k^{th} mode, while $\mathbf{t}$ is the line vector containing the N time-steps. In the present work, $\mathbf{V}_1^N$ consists of both the time response of the load coefficients and the C_p distribution, C_p being span-averaged in the context of DDES results. DMD is then used to reconstruct an approximation of the results. To this end, the most relevant modes $\boldsymbol{\phi}_k^{\text{DMD}}$ are selected by descending order of amplitude q_k^{DMD} and the approximated matrix $\widehat{\mathbf{V}}_1^N$ is then calculated from

$$\widehat{\mathbf{V}}_1^N = \sum_{k^{\text{th}}\text{selected mode}} q_k^{\text{DMD}} \boldsymbol{\phi}_k^{\text{DMD}} \exp\left(\Im\left(\lambda_k^{\text{DMD}}\right)\mathbf{t}\right). \tag{2}$$

The number of selected modes $\boldsymbol{\phi}_k^{\text{DMD}}$ is chosen to obtain statistics computed on $\widehat{\mathbf{V}}_1^N$ similar to those computed on $\mathbf{V}_1^N$. In the following, these modes correspond to the mean mode and the mode $\boldsymbol{\phi}_k^{\text{DMD}}$ associated with the shedding frequency.

3. Results

This section presents and discusses the results obtained experimentally and numerically. Statistics computed on load and pressure coefficients are discussed and compared in Secs. 3.1 and 3.2, respectively. Section 3.3 aims to understand the dynamics of the flow by analysing the time response of the pressure distribution. Finally, Sec. 3.4 studies the effects of the Reynolds number on the flow and the subsequent aerodynamic loads.

3.1. Statistics on the load coefficients and Strouhal number

Figure 4 shows the aerodynamic coefficients and the Strouhal number as a function of the incidence α at $\text{Re} = 1.1 \times 10^4$. Experimental results reported by Nakamura and Mizota (1975) and Washizu et al. (1978) are also depicted for comparison. Note that these authors specified only a range of Reynolds numbers, which are respectively $10^4 \leq \text{Re} \leq 10^5$ and $2\times10^4 \leq \text{Re} \leq 3.3 \times 10^5$, and not a precise value.

Figure 4a plots the mean lift coefficient as a function of the angle of attack. In particular, $\bar{c}_l^{\text{EXP}}$ clearly exhibits a linear increase with α from $-4°$ to $4°$. In this linear region, the slope

$\overline{c}_{l_\alpha}^{\text{EXP}}$ is approximately 2.1π. For $|\alpha| > 5°$, the absolute mean lift coefficient decreases and the rectangular cylinder is stalled. The mean drag coefficient is depicted in Fig. 4b. The variation of $\overline{c}_d{}^{\text{EXP}}$ exhibits a classical parabolic variation for absolute angles lower than 4°. For higher incidence, as the rectangular cylinder is stalled (decrease of lift), the increase in drag saturates. Finally, as shown in Fig. 4c, the variation of the mean pitching moment about the center of the rectangular cylinder exhibits a linear decrease for incidence $|\alpha| \leq 2°$. The corresponding slope is $\overline{c}_{m_\alpha}^{\text{EXP}} \approx -0.35\pi$. This linear behavior is followed by a saturation. For $|\alpha| > 5°$, the absolute $\overline{c}_m{}^{\text{EXP}}$ decreases slightly again. Finally, the Strouhal number is shown in Fig. 4d. For $-3° < \alpha < 3°$, St^{EXP} is nearly constant and equal to 0.134. Then, for increasing incidence, St^{EXP} decreases linearly to reach $\text{St}^{\text{EXP}} = 0.116$ for $\alpha = 8°$.

The mean aerodynamic coefficients are compared to experimental results available in the literature. The slope $\overline{c}_{l_\alpha}^{\text{EXP}}$ is relatively close to the value reported by Washizu et al. (1978) ($\overline{c}_{l_\alpha} = 2.3\pi$) but very different from the result of Nakamura and Mizota (1975) ($\overline{c}_{l_\alpha} = 3.3\pi$). As mentioned in Sec. 1 and later illustrated in Sec. 3.4, the mean lift slope can be very sensitive to the Reynolds number. However, as the Reynolds number associated with these works from the literature is not known precisely, no conclusion can be drawn. The stall angle is similar for the three sets of results. However, the post-stall decrease in $\overline{c}_l$ is higher for the results presented by Nakamura and Mizota (1975) and even higher for the experiments carried out by Washizu et al. (1978). The mean drag $\overline{c}_d$ at zero incidence is identical for the two studies from the literature. However, this value is higher by 0.1 compared to $\overline{c}_d{}^{\text{EXP}}$. For incidences $|\alpha| < 4°$, the parabolic shape exhibited by the curve $\overline{c}_d{}^{\text{EXP}}$ is similar to the one obtained by Washizu et al. (1978), but the results reported by Nakamura and Mizota (1975) show a stronger increase of the drag with the incidence. Some of those discrepancies can be explained by the difference in the load acquisition process, as Nakamura and Mizota (1975) and Washizu et al. (1978) used strain-gauges which include the friction drag to measure the forces. As shown by Carassale et al. (2014) and Wang and Gu (2015), rounded cross-section corners lead to a decrease of the drag. Therefore, another source of discrepancy could be the sharpness of the model edges. Moreover, the number of pressure tabs available along the front and rear surfaces might be insufficient to obtain sufficient accurate drag estimates. Finally, the variation of $\overline{c}_m{}^{\text{EXP}}$ with α is comparable to the results reported by Nakamura and Mizota (1975). In particular, the slope in the linear part of the curves and the saturation behavior are similar.

Figure 4 also compares the mean load coefficients and the Strouhal number obtained experimentally and numerically. In particular, Fig. 4a shows that the mean lift coefficient $\overline{c}_l{}^{\text{URANS}}$ increases linearly with the angle of attack α until $\alpha = 3°$. Beyond this value, the lift coefficient keeps increasing, but at a decreasing rate. The discrepancies with the experimental curve $\overline{c}_l{}^{\text{EXP}}$ are very large as both the URANS estimated slope $\overline{c}_{l_\alpha}$ and the behavior in the post-stall region differ dramatically. The slope $\overline{c}_{l_\alpha}^{\text{URANS}}$ is equal to 3.9π which is nearly twice the measured one. This slope is also very different from the result documented by

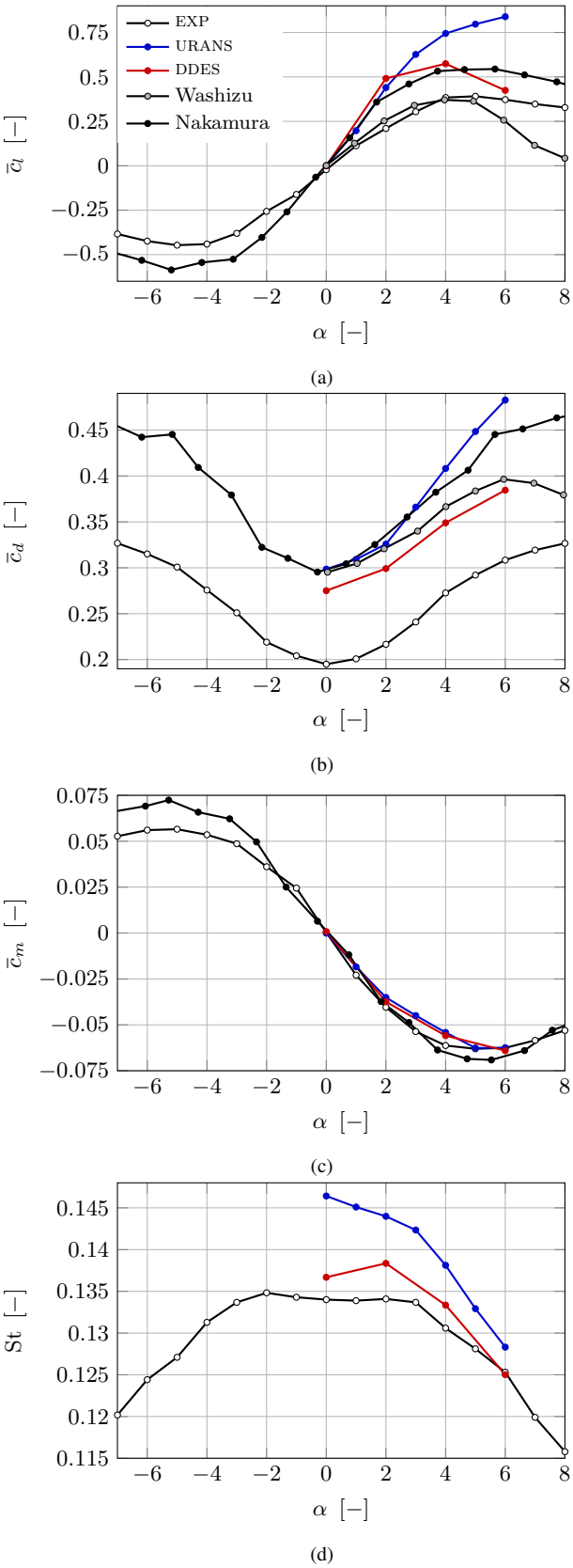

Figure 4: Mean of the aerodynamic coefficients (a, b and c) and Strouhal number (d) obtained experimentally and by CFD as a function of the angle of attack at $\text{Re} = 1.1 \times 10^4$. Experimental results of Nakamura and Mizota (1975) and Washizu et al. (1978) from direct load measurements are included for comparison.

Washizu et al. (1978). However, for incidences lower than 2°, $\overline{c}_{l_\alpha}^{\text{URANS}}$ is similar to the results presented by Nakamura and Mizota (1975). Additionally, the behavior for angles of attack higher than 3° is not correctly captured by the URANS model, as the lift curve does not exhibit any stall region for the considered range of incidences but only a monotonic increase at a decreasing rate. The $\overline{c}_d^{\text{URANS}}$ curve shown in Fig. 4b exhibits the expected quadratic behavior. The most visible discrepancy is the constant shift up of $\overline{c}_d^{\text{URANS}}$ compared to $\overline{c}_d^{\text{EXP}}$. However, as discussed previously, it is preferable to compare $\overline{c}_d^{\text{URANS}}$ with the results documented by Nakamura and Mizota (1975) and Washizu et al. (1978), for which the discrepancies are lower. In particular, for incidences lower than 2°, $\overline{c}_d^{\text{URANS}}$ approximates fairly accurately the literature results. For larger angles of attack, URANS simulations overestimate the mean drag coefficient, this overestimation increasing with incidence. The dependence of the mean moment coefficient $\overline{c}_m^{\text{URANS}}$ on α in Fig. 4c is in agreement with the experimental results. Finally, as shown in Fig. 4d, the Strouhal number exhibits an initial linear decrease until $\alpha = 3°$, followed by a second faster linear decrease. Compared to the experimental results, the URANS Strouhal is higher at all angles of incidence. Nonetheless, a modification of the slope at $\alpha = 3°$ is also observed experimentally, although the value of the slopes differs quantitatively.

The DDES predictions are an improvement upon the URANS estimates but discrepancies with the experimental results still remain. Figure 4a shows that the slope $\overline{c}_{l_\alpha}^{\text{DDES}} \approx 4.5\pi$ is even higher than the already too high slope calculated by URANS. Nonetheless, DDES simulations lead to a better behavior of $\overline{c}_l$ for incidence angles higher than 2°. In particular, a stall region characterized by a decrease in lift is captured but the estimated lift is still too high compared to the experimental results. Moreover, Fig. 4b shows that DDES simulations lead to a better estimation of $\overline{c}_d$ than URANS for incidence angles higher than 2°. As shown in Fig. 4c, the mean pitching moment coefficient $\overline{c}_m^{\text{DDES}}$ is estimated with reasonable accuracy compared to the experimental measurements. Finally, as depicted in Fig. 4d, the estimation of the Strouhal number is also improved by the use of DDES, although the plateau observed in EXP results for $0° < \alpha < 3°$ is not perfectly captured.

In conclusion, the URANS approach is not able to estimate $\overline{c}_l$ with a reasonable accuracy, neither to accurately predict the stall angle. Nevertheless, it demonstrates a reasonable ability to estimate the drag below the stall angle and it provides an accurate estimation of the mean pitching moment. DDES yields better predictions for incidence angles in the stall region. The stall angle is correctly captured and the estimated lift is closer to the experimental values for post-stall incidences. However, the estimation of $\overline{c}_{l_\alpha}^{\text{DDES}}$ is even worse than the URANS results. In order to explain these discrepancies, the next sections analyze the pressure coefficient distributions C_p obtained experimentally and numerically.

3.2. Statistics on the pressure coefficient

The discrepancies between the simulated and experimental aerodynamic loads presented in the previous section are explained here by means of a statistical analysis of the pressure distribution. First, the experimental C_p distribution is presented for several angles of attack for $\text{Re} = 1.1 \times 10^4$. Then, the comparison with the simulation results (URANS and DDES) is carried out.

3.2.1. Experimental results

Figure 5 depicts the mean and standard deviation of C_p^{EXP} for angles of attack in the range $0° \leq \alpha \leq 6°$. The distributions along the upper and lower surfaces of the rectangular cylinder are represented by plain and dashed lines, respectively. For the sake of clarity, $\overline{C}_p$ is not depicted along the upstream face but it exhibits the expected parabolic behavior around $\overline{C}_p = 1$.

At zero incidence, the distribution of $\overline{C}_p^{\text{EXP}}$ is nearly identical for the upper and lower surfaces. Starting from the leading edges of the cylinder, the pressure is almost constant with only a very weak decrease over the first half of the upper and lower surfaces. It then increases rapidly but smoothly until the rear side of the rectangular cylinder. The start of this pressure recovery is located at around $\overline{r} = 0.5$. This location corresponds to the core of a vortex referred to as the main vortex by Bruno et al. (2010) and appearing along both the upper and lower sides. In particular, this main vortex is enclosed in a mean separation bubble extending from the leading edge of the cylinder to the point where the mean free shear layer impinges on the surface and the flow reattaches. The maximum of $\overline{C}_p$ along the upper and lower surfaces is located at a distance $0.94c$ from the leading edges. As shown by Robertson et al. (1975, 1978) and illustrated in Sec. 3.2.2, this location correlates with the point where the mean flow reattachment occurs (Mannini et al., 2017), i.e. the end of the main vortex

For non-zero incidences, increasing the angle of attack extends the plateau region on the upper surface further downstream and reduces the magnitude of the pressure recovery. Additionally, the pressure intensity of the $\overline{C}_p^{\text{EXP}}$ plateau region remains more or less the same for small angles of attack. As these changes in the pressure distribution can be related to changes in the mean flow structures, this shows that the main vortex core moves downstream on the upper surface as α increases. Moreover, as $\overline{C}_p^{\text{EXP}}$ does not exhibit a local maximum near the trailing edge of the cylinder, it is possible that the mean flow does not reattach along the upper surface for $\alpha \geq 2°$. At $\alpha = 4°$, the suction in the nearly constant $\overline{C}_p$ region slightly decreases, which corresponds to the end of the linear region of the $\overline{c}_l^{\text{EXP}}$ curve shown in Fig. 4a. At $\alpha = 6°$, the distribution of $\overline{C}_p^{\text{EXP}}$ is nearly flat over the entire upper surface and its magnitude is significantly reduced compared to lower angles of attack. This is typical for a post-stall angle and explains the decrease of the mean lift coefficient $\overline{c}_l^{\text{EXP}}$. The opposite behavior is observed on the lower surface. The extent of the plateau region and the corresponding suction decrease with increasing angle of attack. Moreover, the pressure recovery is more abrupt and reaches a maximum value that increases and whose location moves upstream with α. This behavior suggests that the mean reattachment point moves upstream with increasing angle, while the mean separation bubble lying along the lower surface shortens.

The second order statistic C'_p represents the temporal varia-

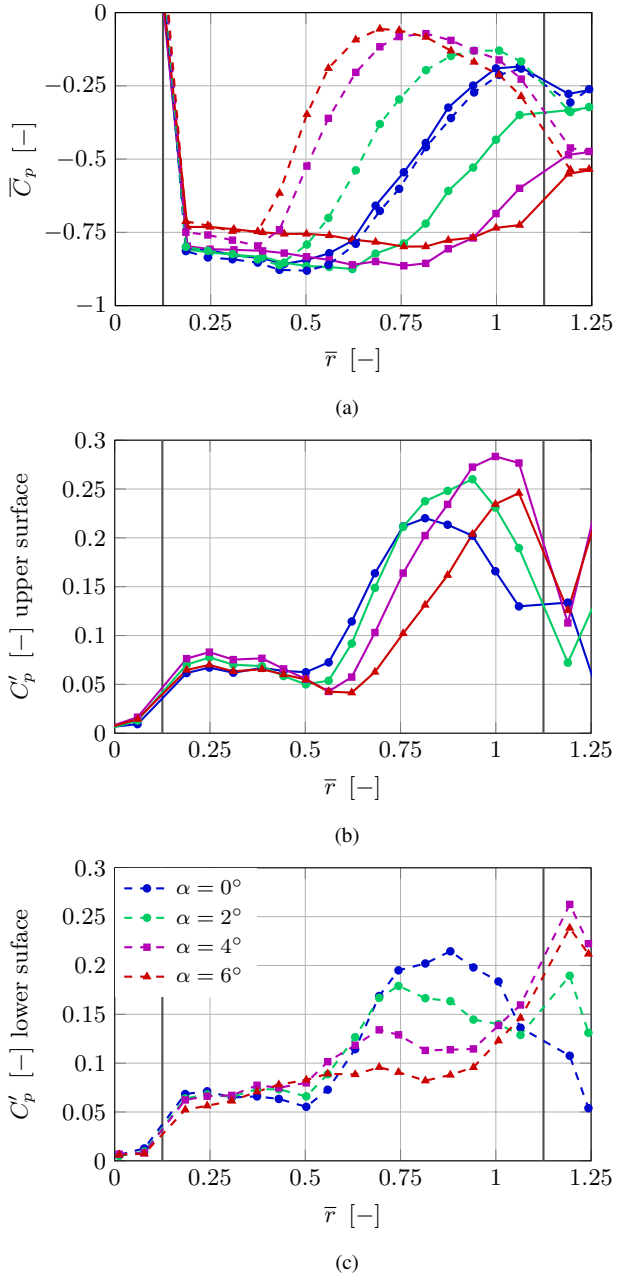

Figure 5: Mean (a) and standard deviation (b and c) of the pressure coefficient C_p along the rectangle surface obtained experimentally at $\mathrm{Re} = 1.1 \times 10^4$ for different angles of attack. The vertical gray lines represent the leading and trailing edges and the coordinate $\overline{r}$ is defined in Fig. 2.

tion around $\overline{C}_p$. Therefore, a high standard deviation along a particular region is representative of unsteady flow separation. As depicted in Fig. 5b, the distribution of $C'^{\,\mathrm{EXP}}_p$ along the upper surface can be divided into two main parts: a region with low standard deviation from the leading edge to $\overline{r} \approx 0.6$, followed by rapid increase and large values of C'_p up to the trailing edge. The standard deviation reaches a maximum in this second region. Increasing the incidence extends the first region further downstream and moves the location of the maximum C'_p closer to the trailing edge. The value of this maximum also increases until $\alpha = 4°$, and then decreases for post-stall angles of attack. The same two regions are also present on the lower surface, as shown in Fig. 5c. Increasing the angle of attack has however the opposite effects.

3.2.2. *Comparison between experimental and* CFD *results*

Figure 6 depicts the $\overline{C}_p$ distributions obtained through URANS and DDES. Experimental results are also shown for comparison purposes. The streamlines of the mean flow obtained by URANS and DDES are also depicted.

As shown in Fig. 6a for 0° angle of attack, two symmetric vortices denoted A_U and A_L lie along the upper and lower surfaces, respectively. The flow reattachment point is located at a distance $0.92c$ from the leading edge for URANS and $0.94c$ for DDES. A distribution similar to $\overline{C}_p^{\,\mathrm{EXP}}$ is obtained with URANS. The main difference is a shift down of $\overline{C}_p^{\,\mathrm{URANS}}$ compared to the experimental distribution. Moreover, the numerically computed pressure recovery begins slightly further from the leading edge and the suction minimum occurs slightly downstream. These differences can be explained by discrepancies in the estimation of the mean flow features. In particular, it seems that the URANS vortex core of A_U and A_L and the reattachment points are located slightly downstream compared to the presumed experimental locations. As shown by Wang and Gu (2015), this could be explained by the sharpness of the lower edge of the experimental model compared to the numerical geometry. On the other hand, the shape of $\overline{C}_p^{\,\mathrm{DDES}}$ significantly differs from $\overline{C}_p^{\,\mathrm{EXP}}$. In particular, the plateau region is followed by a zone where the suction increases before the pressure recovery and the pressure recovery begins at a location much further downstream than for other results. These discrepancies are caused by differences in the shape of the mean vortices A_U and A_L. As shown by the streamlines, the mean vortex cores are located further downstream than for URANS, which delays the pressure recovery. Additionally, the vortices are more tilted than for other CFD results. Therefore, the curvature of the mean streamlines is more important below the vortex cores, which explains the suction peak at $\overline{r} = 0.75$. Finally, the mean streamlines can be compared to the literature results. The URANS streamlines are similar to the experimental results obtained by Mizota (1981) for a similar case. In particular, the reattachment of the flow occurs at the same location. However, this experimental study reports a slightly thinner vortex with a core located at $\overline{r} \approx 0.53$, i.e., slightly further upstream than for URANS. Conversely, the mean streamlines computed with DDES are very different as the principal axis of the main vortex is too tilted and its core is located too far downstream.

At larger angles of attack, vortex A_U grows and moves downstream, as seen in Figs. 6b to 6d ($\alpha = 2°$, 4° and 6°). From $\alpha = 2°$ the flow does not reattach along the upper surface, and for $\alpha \geq 4°$, vortex A_U wraps around the trailing edge. Conversely, vortex A_L shrinks and is located further upstream, so that the reattachment point moves forward. This behavior is consistent with the conclusions drawn in Sec. 3.2.1. The mean pressure distribution along the lower surface estimated by URANS is similar to $\overline{C}_p^{\,\mathrm{EXP}}$, despite an underestimation of the suction due to vortex A_L for $\alpha > 2°$. On the other hand, $\overline{C}_p^{\,\mathrm{DDES}}$ is

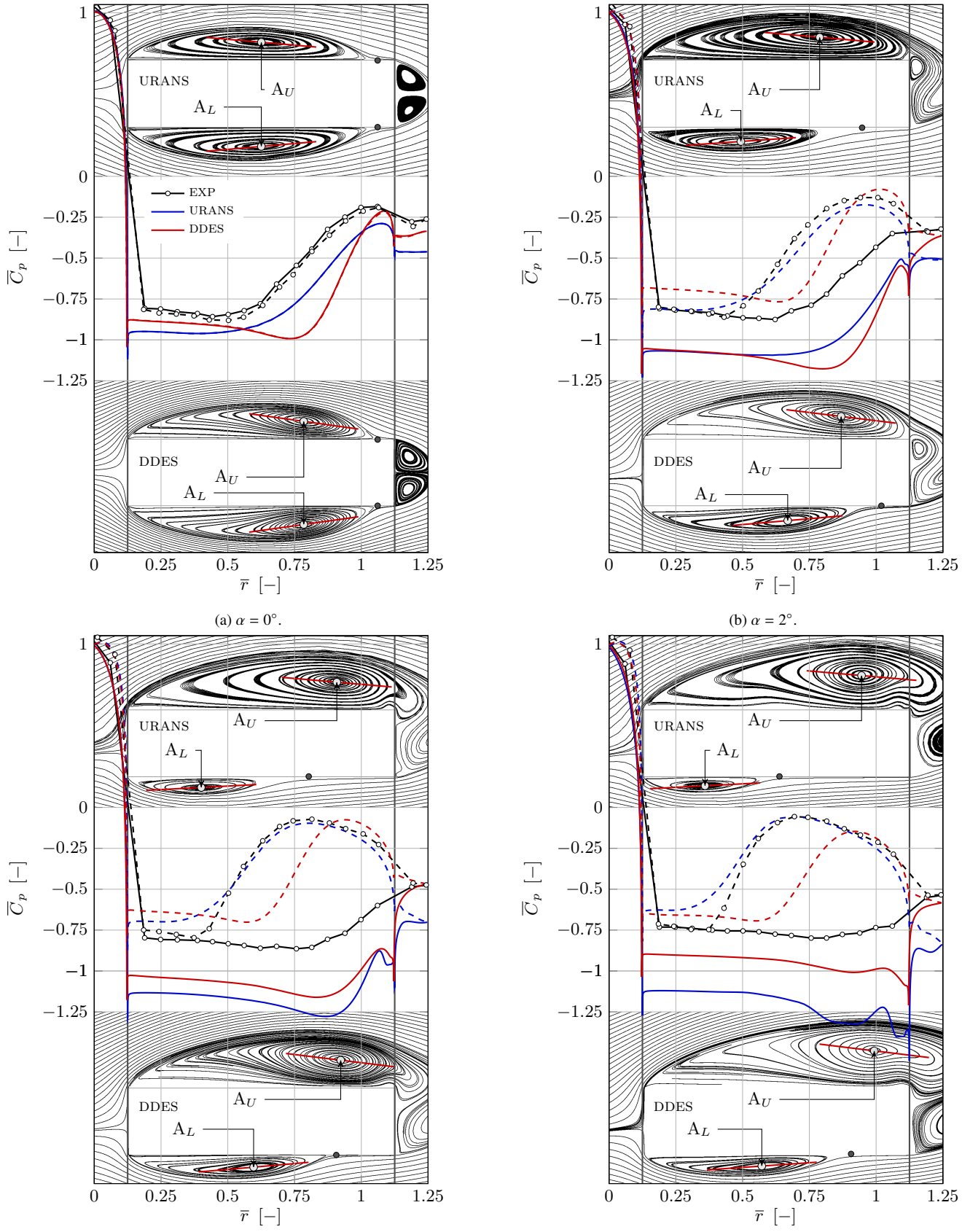

(a) $\alpha = 0°$.

(b) $\alpha = 2°$.

(c) $\alpha = 4°$.

(d) $\alpha = 6°$.

Figure 6: Streamlines of the mean flow calculated by CFD and mean pressure coefficient C_p along the rectangle surface obtained by URANS, DDES and experimentally (EXP) at Re = 1.1×10^4 for different angles of attack. Plain and dashed lines correspond to the upper and lower surface, respectively. The light gray disk corresponds to the main vortex core and the dark gray one to the reattachment point. The red line represents the principal axis of the main vortex.

very different from the experimental results, as the pressure recovery begins significantly downstream. This shift is due to the reattachment point and the vortex core of A_L that are estimated too far downstream. The numerically computed $\overline{C}_p$ along the upper surface is very different from $\overline{C}_p^{\text{EXP}}$. The suction intensity is largely overestimated, which causes the overestimation of $\overline{c}_l$ discussed in Sec. 3.1. Nonetheless, for $2° \leq \alpha \leq 4°$, the global shape of $\overline{C}_p^{\text{EXP}}$ along the upper surface is correctly predicted by URANS. In particular, the pressure recovery and thus the location of the core of vortex A_U are fairly well estimated. For $2° \leq \alpha \leq 6°$, the pressure recovery of $\overline{C}_p^{\text{CFD}}$ along the upper surface exhibits a non-monotonous behavior just before the trailing edge. This modification in the trend of $\overline{C}_p$ is caused by a small counter-rotating vortex highlighted by Mannini et al. (2017) which cannot be detected experimentally because of the limited number of pressure taps. At $\alpha = 6°$, the flow along the upper surface is better estimated by DDES, as Fig. 6d shows a decrease of the suction intensity compared to 4° (Fig. 6c). This decrease in suction is also observed for $\overline{C}_p^{\text{EXP}}$ (see Sec. 3.2.1) and causes a decrease of the lift for incidence angles higher than the stall angle. Moreover, the $\overline{C}_p^{\text{DDES}}$ distribution is nearly flat, which is also the case for the experimental results. Conversely, the suction intensity of $\overline{C}_p^{\text{URANS}}$ is similar for 4° and 6°. Therefore, $\overline{c}_l^{\text{URANS}}$ does not decrease for $\alpha > 4°$ and URANS is not able to predict the stall angle.

For the sake of conciseness, the standard deviations of C_p obtained through CFD are not shown. Nonetheless, the comparison between numerical and experimental results demonstrates that the general shapes of C'_p depicted in Fig. 5 are overall retrieved as long as the chordwise location of the vortex core is accurately captured. However, the amplitude of C'_p is largely overestimated by CFD. Moreover, URANS results show a non-physical minimum of C'_p. These two aspects were also reported by Patruno et al. (2016).

3.3. Spatio-temporal pressure coefficient and flow dynamics

This section aims to better understand the dynamics of the flow by analyzing the time response of the pressure distribution. Both experimental and numerical results are considered and their respective C_p values are compared over a shedding cycle in Sec. 3.3.1. The flow dynamics is then described in Sec. 3.3.2.

3.3.1. Comparison between experimental and CFD results

The experimental and numerical C_p are compared through their respective approximation $\widehat{C_p}$, which is obtained from a reconstruction based on the first two DMD modes, as explained in Sec. 2.3. The spatio-temporal variation of $\widehat{C_p}$ is shown for $\alpha = 0°$ and 2° in Figs. 7 and 8. They depict $\widehat{C_p}$ at four different phases $\varphi = t/T$, where t and T are the time and the shedding period, respectively. The beginning of a cycle, i.e., $\varphi = 0$, corresponds to the minimum of $\widehat{c_l}^{\text{EXP}}$. The figures also show the URANS streamlines of the original flow field corresponding to each phase.

Figure 7 presents the results for 0° of incidence. As the flow field is symmetrical, the accuracy of the shedding phenomenon obtained numerically is assessed by comparing the variation of $\widehat{C_p}^{\text{EXP}}$ and $\widehat{C_p}^{\text{CFD}}$ along the upper surface only. The dynamics along the lower surface is very similar but distant in time by half a cycle. One can first observe that the URANS simulation predicts better than DDES the variation of pressure, despite a consistent larger suction on the entire upper and lower surfaces. Additionally, the pressure recovery starts very slightly further downstream at $\varphi = 0.25$ and $\varphi = 0.5$. As already observed for the mean flow, DDES results display much larger discrepancies with a larger suction peak and a pressure recovery displaced downstream. This is due to a larger and more tilted vortex A_U^1, whose core is located further downstream. Finally, the numerical results show larger variations in time, explaining the larger standard deviation obtained with CFD.

For larger angles of attack (Fig. 8 for $\alpha = 2°$), the URANS predictions are qualitatively more similar to the experimental results than the DDES estimates, but the quantitative discrepancies increase with the incidence angle. This is especially the case on the upper surface where suction is highly overestimated. On the other hand, DDES results show larger qualitative and quantitative discrepancies. The better qualitative agreement between URANS and experiments, especially regarding the chordwise location of the vortex cores and of the reattachment points, indicates that URANS also provides a better representation of the flow dynamics at larger angles of attack. However, at $\alpha = 6°$ (not shown here), significant discrepancies appears between URANS and experimental results along the upper surface and URANS is not able to correctly predict the flow above the rectangular cylinder.

3.3.2. Flow dynamics

The relatively good qualitative agreement between URANS and experimental results suggests that URANS is better at representing the flow dynamics for $\alpha < 6°$. Therefore, the dynamic phenomena can be qualitatively understood by analyzing the flow computed by URANS. In particular, Figs. 9 and 10 show the variation of the flow around a rectangular cylinder at 0° and 2° of incidence during a shedding cycle.

At 0° of incidence, the flow topology above and below the horizontal symmetry axis of the rectangle is identical but occurs at times distant by half a shedding period. Therefore, the entire dynamics is described by the time response of the flow above the upper surface for $0 \leq \varphi \leq 0.5$, and then by the flow below the lower surface, starting back at $\varphi = 0$. At $\varphi = 0$, and as depicted by streamlines in Fig. 9a, a large clockwise rotating vortex, called vortex A_U^1, lies along the upper surface. The vorticity plot shows that the free shear layer does not impinge on the rear part of the upper surface, although the flow reattaches. Instead, it extends in the wake up to a zone of low pressure corresponding to a previously shed vortex denoted D_U^0, as depicted in Fig. 9b. As shown in Fig. 9c, vortex A_U^1 is then convected downstream while the free shear layer moves closer to the surface. A clockwise rotating zone lies along the rear part of the upper surface and rolls around the upper trailing edge of the cylinder, forming a small vortex denoted B_U^0. While vortex A_U^1 is being stretched and convected downstream, a new vortex A_U^2 forms at the leading edge of the cylinder. The emergence of this vortex is recognizable by the drop in pressure coefficient

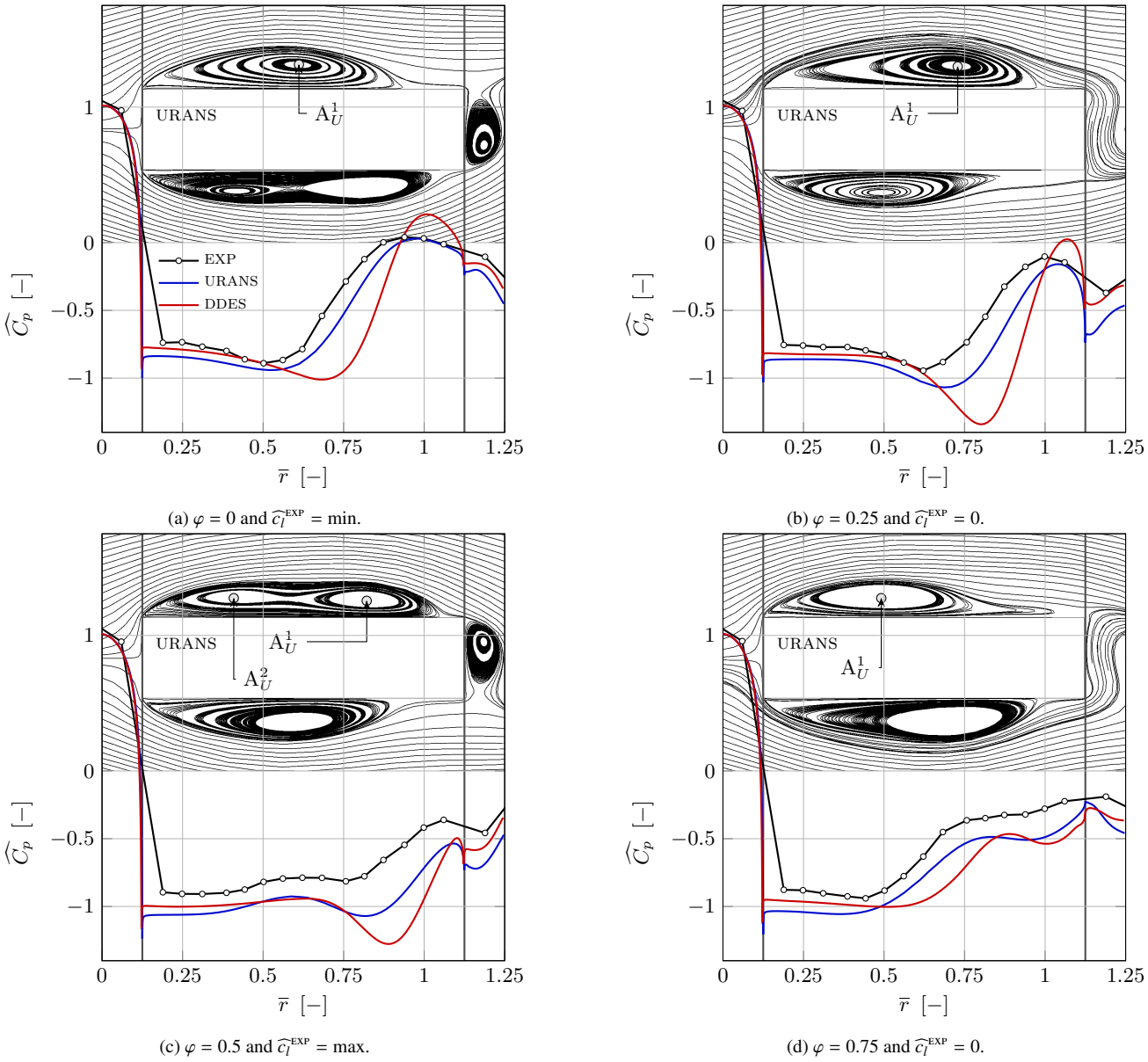

(a) $\varphi = 0$ and $\widehat{c_l}^{\text{EXP}} = \min$.

(b) $\varphi = 0.25$ and $\widehat{c_l}^{\text{EXP}} = 0$.

(c) $\varphi = 0.5$ and $\widehat{c_l}^{\text{EXP}} = \max$.

(d) $\varphi = 0.75$ and $\widehat{c_l}^{\text{EXP}} = 0$.

Figure 7: Distribution of the pressure coefficient reconstructed from the first two DMD modes at four different phases of the shedding cycle for the flow around a rectangular cylinder at $\alpha = 0°$ and $\text{Re} = 1.1 \times 10^4$. Plain lines correspond to the upper surface. The streamlines of the original flow field obtained from URANS are also represented for easier interpretation.

near the leading edge shown in Fig. 9f. Vortex A_U^2 then grows, pushing vortex A_U^1 further downstream (lower part of Figs. 9a and 9b), where $A_L^0 = A_U^1$ and $A_L^1 = A_U^2$. At the same time, the free shear layer impinges on the upper rear corner, feeding vortex B_U^0 (= B_L^0), which also grows and starts to detach from the rear surface. As depicted in Figs. 9c and 9d, where $D_L^0 = D_U^1$, vortices A_U^1 and B_U^0 eventually merge into a single vortex D_U^1, which is shed into the wake. Only vortex A_U^2 remains on the upper surface. Finally, vortices A_U^2 and D_U^1 are convected downstream and a new cycle resumes.

Figure 10a shows an overview of the flow at an incidence of 2°. A large clockwise rotating vortex called vortex A_U^1 covers nearly the entire upper surface at $\varphi = 0$ (Figs. 10a and 10b). The free shear layer follows the upper part of vortex A_U^1 and extends into the wake until the location of a vortex called A_U^0. Moreover, a small counter-clockwise vorticity zone lies at the upper trailing edge indicating the presence of a vortex called B_U^0. The same phase shows the emergence of a conter-clockwise rotating vortex called A_L^1 at the leading edge of the lower surface. Moreover, another vortex called A_L^0 and previously generated at the leading edge is still visible on the rear part of the lower surface. The free shear layer along vortices A_L^0 and A_L^1 impinges on the rear part of the lower surface. This shear layer extends further downstream, rolling around the lower trailing edge and feeding the counter-clockwise rotating vortex B_L^0 behind the rectangle. As shown in Figs. 10c and 10d, vortex A_U^1 elongates downstream while the upper shear layer impinges the upper trailing edge and vortex B_U^0 is dissipated. On the lower

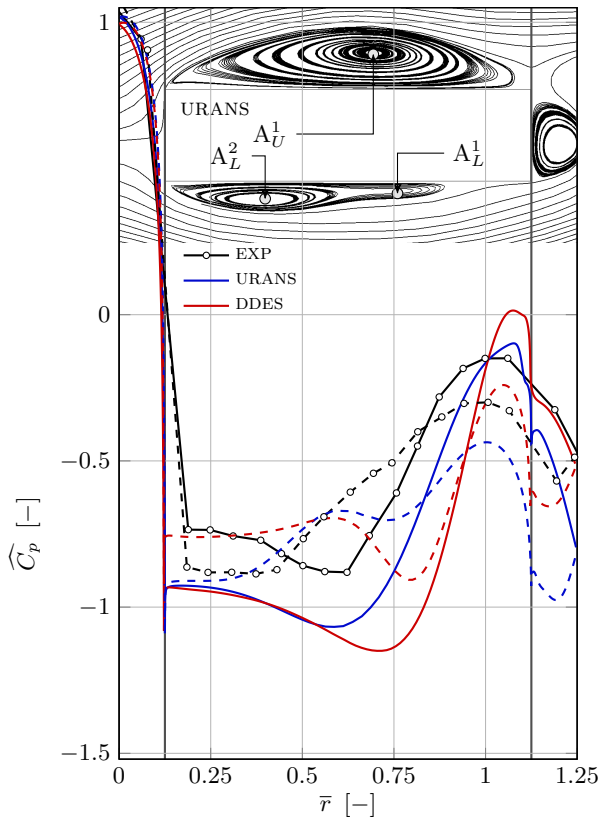

(a) $\varphi = 0$ and $\widehat{c_l}^{\text{EXP}} = \text{min}$.

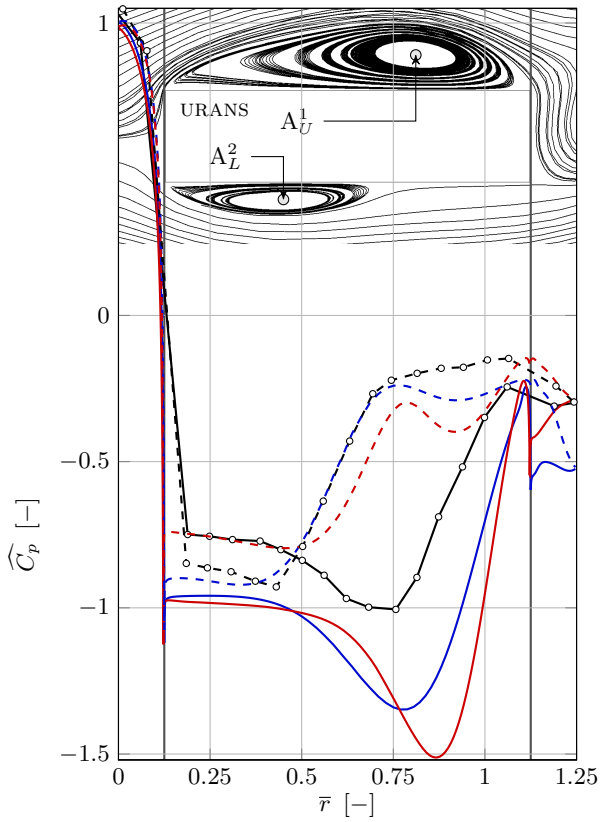

(b) $\varphi = 0.25$ and $\widehat{c_l}^{\text{EXP}} = 0$.

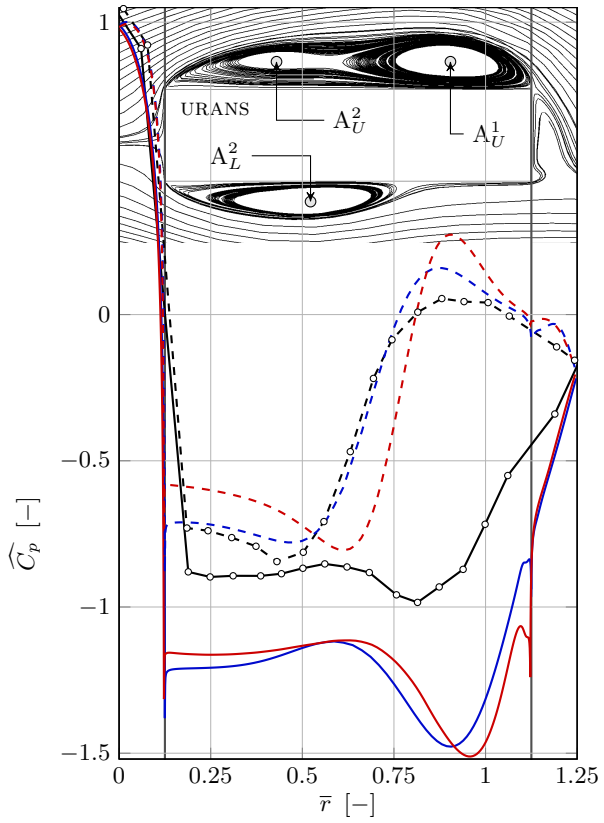

(c) $\varphi = 0.5$ and $\widehat{c_l}^{\text{EXP}} = \text{max}$.

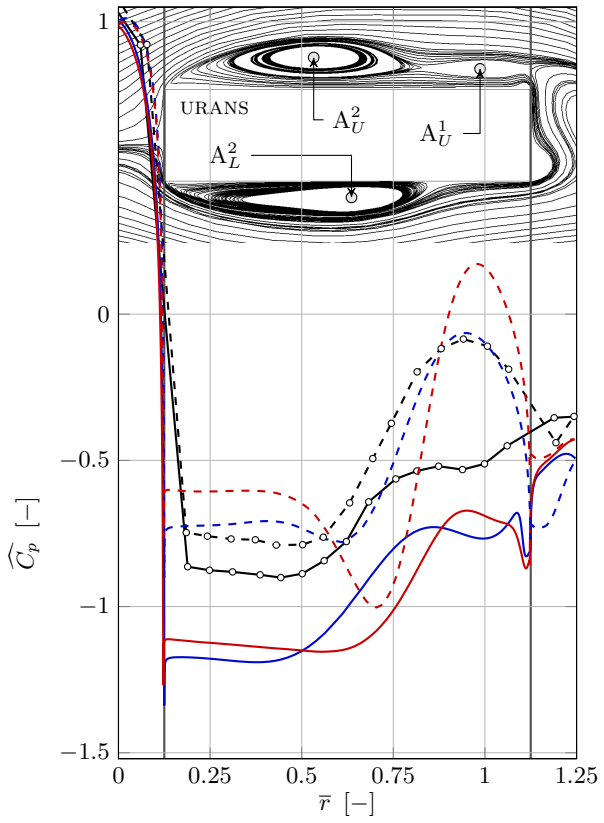

(d) $\varphi = 0.75$ and $\widehat{c_l}^{\text{EXP}} = 0$.

Figure 8: Distribution of the pressure coefficient reconstructed from the first two DMD modes at four different phases of the shedding cycle for the flow around a rectangular cylinder at $\alpha = 2°$ and $\text{Re} = 1.1 \times 10^4$. Plain and dashed lines correspond to the upper and lower surface, respectively. The streamlines of the original flow field obtained from URANS are also represented for easier interpretation.

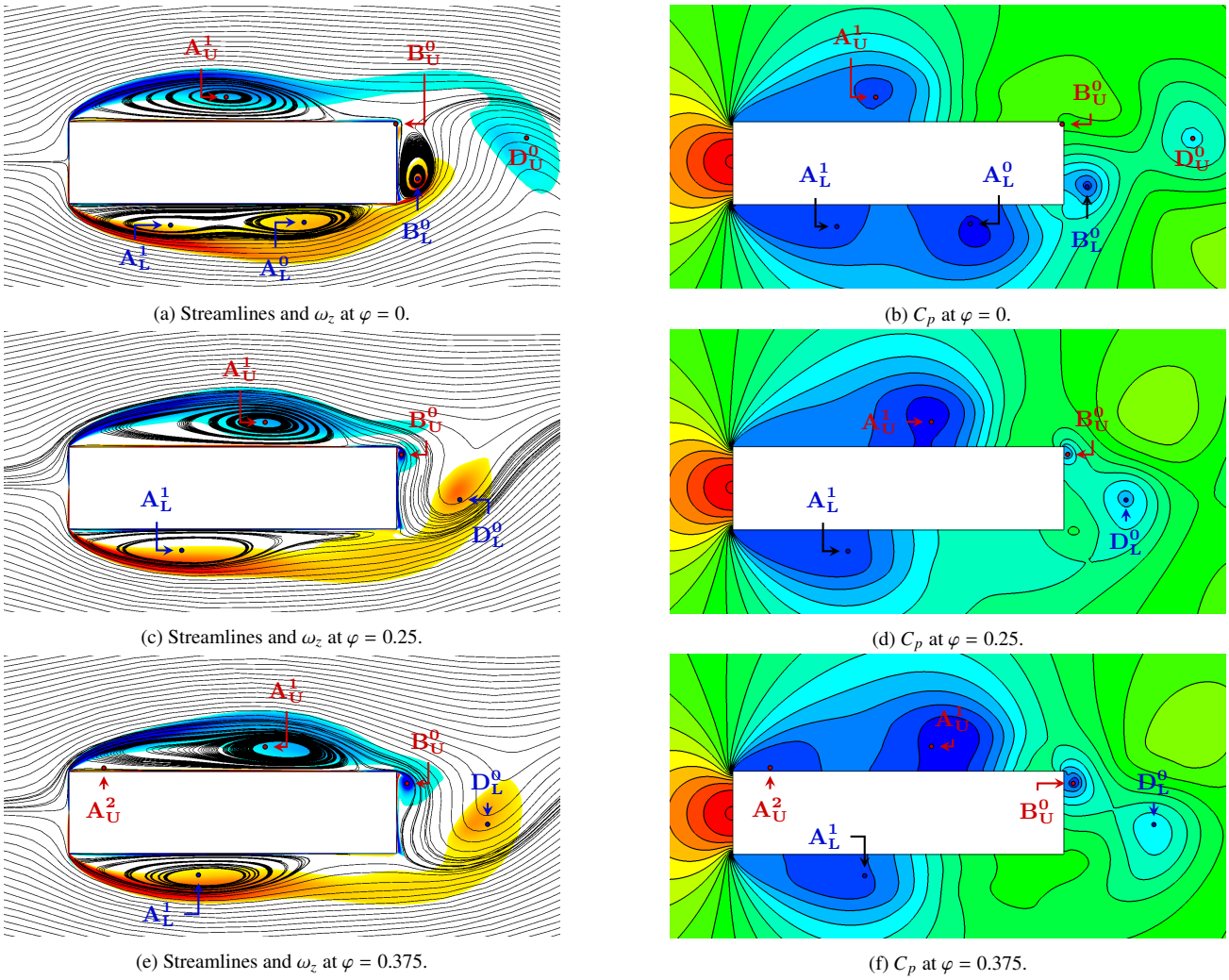

(a) Streamlines and ω_z at $\varphi = 0$.

(b) C_p at $\varphi = 0$.

(c) Streamlines and ω_z at $\varphi = 0.25$.

(d) C_p at $\varphi = 0.25$.

(e) Streamlines and ω_z at $\varphi = 0.375$.

(f) C_p at $\varphi = 0.375$.

Figure 9: Evolution within a vortex shedding cycle of the flow around a rectangular cylinder at 0° and Re = 1.1×10^4 obtained by URANS. Left column: streamlines and vorticity (clockwise in blue and counter-clockwise in red). Right column: pressure coefficient C_p (high pressure in red and low pressure in blue) and associated iso-contours.

surface, vortices A_L^1 is convected downstream while vortex A_L^0 and B_L^0 merge into a single vortex called D_L^0 which is shed into the wake. At $\varphi = 0.5$ (Figs. 10e and 10f), a new vortex A_U^2 forms at the upper leading edge. The upper shear layer rolls around vortex A_U^1 and the upper trailing edge, impinging the rear surface. Along the lower surface, vortex A_L^1 is convected downstream and the free shear layer moves further away from the surface. Simultaneously, a counter-clockwise vorticity zone starts to form and grows into a vortex B_L^1 at the lower trailing edge. This vortex appears clearly in Figs. 10g and 10h corresponding to $\varphi = 0.75$. At this stage, vortex A_L^1 lies alone on the lower surface. A counter-clockwise rotating vortical zone grows at the trailing edge of the upper surface and forms a small vortex B_U^1 while vortex A_U^2 keeps growing. Simultaneously, vortex A_U^1 becomes weaker as it extends progressively from the rear part of the upper surface into the wake. Vortex A_U^1 is finally completely shed at the end of the cycle (see vortex A_U^0 in Figs. 10a and 10b).

To summarize, the main dynamics consists for both cases in the emergence of a vortex at the leading edge. This vortex grows and is convected downstream along the surface until it reaches the rear part of the cylinder and is shed into the wake. However, at 0° of incidence, the vortex generated at the leading edge merges with another vortex that has grown at the trailing edge. The merged vortex is then shed into the wake. For an incidence of 2°, the dynamics of the flow structures is similar along the lower surface. However, it differs along the upper surface where the vortex generated at the leading edge is convected and shed into the wake without merging with the vortex that has appeared at the trailing edge.

3.4. Reynolds number effects

This section studies the effects of the Reynolds number on the flow by analyzing the changes in the mean lift coefficient, its slope and in the statistics of the pressure coefficient.

The mean lift coefficient $\overline{c}_l^{\text{EXP}}$ is represented for $\alpha = 2°$ and $\alpha = 4°$ and several Reynolds numbers in Fig. 11, that also depicts the lift slope $\overline{c}_{l_\alpha}^{\text{EXP}}$ calculated between $\alpha = 0°$ and 2°. Figure 11 illustrates that an increase of the Reynolds number in

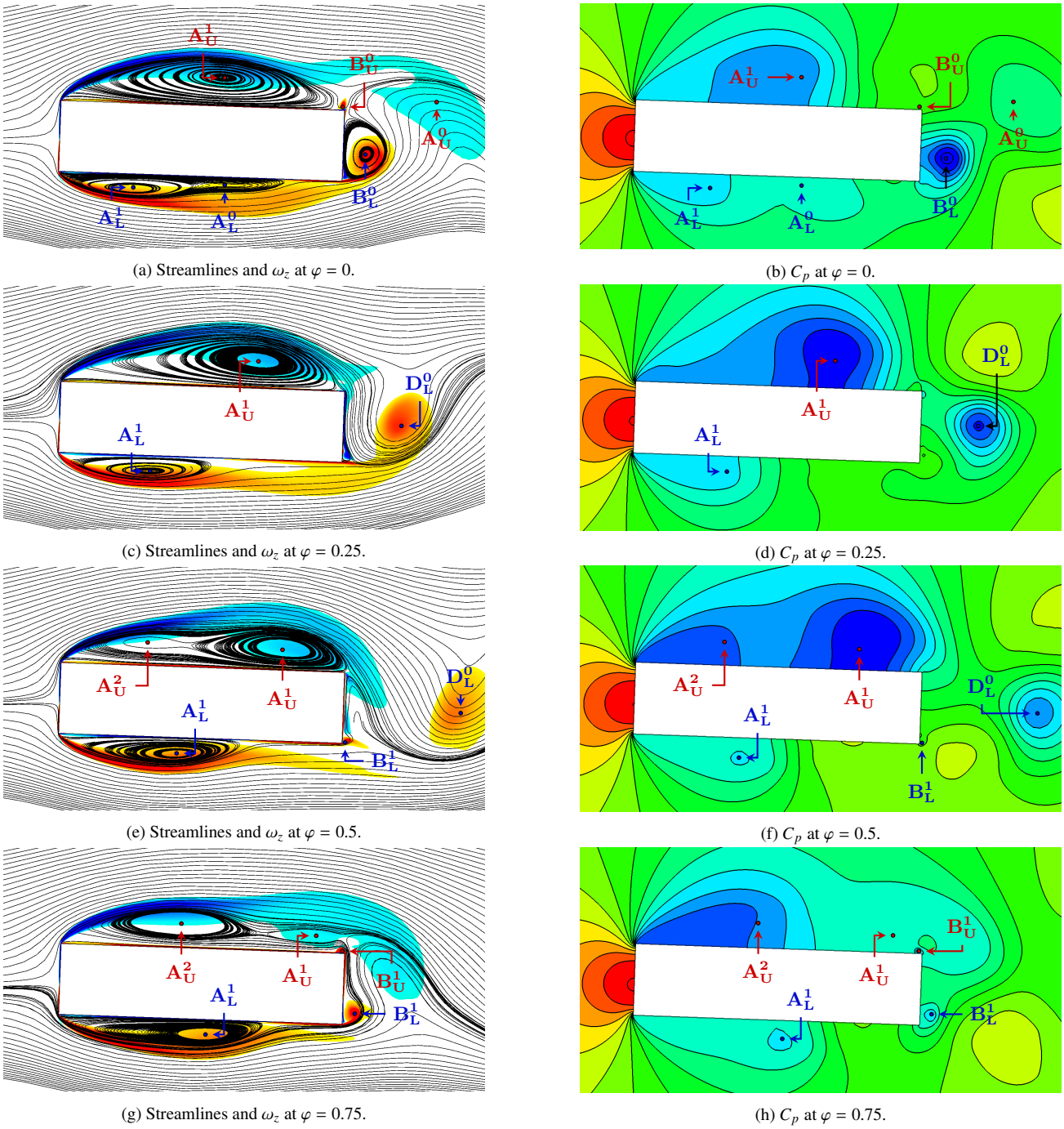

(a) Streamlines and ω_z at $\varphi = 0$.

(b) C_p at $\varphi = 0$.

(c) Streamlines and ω_z at $\varphi = 0.25$.

(d) C_p at $\varphi = 0.25$.

(e) Streamlines and ω_z at $\varphi = 0.5$.

(f) C_p at $\varphi = 0.5$.

(g) Streamlines and ω_z at $\varphi = 0.75$.

(h) C_p at $\varphi = 0.75$.

Figure 10: Evolution within a vortex shedding cycle of the flow around a rectangular cylinder at 2° and Re = 1.1×10^4 obtained by URANS. Left column: streamlines and vorticity (clockwise in blue and counter-clockwise in red). Right column: pressure coefficient C_p (high pressure in red and low pressure in blue) and associated iso-contours.

the range considered here leads to a significant increase of the slope $\overline{c}_{l_\alpha}^{\text{EXP}}$. In particular, increasing the Reynolds number from 7.7×10^3 to 1.9×10^4 leads to a relative increase of 45% of the slope. This is consistent with the results reported by Schewe (2013) for a 5:1 rectangular cylinder. More precisely, Schewe (2013) showed a significant increase of $\overline{c}_{l_\alpha}$ when increasing the Reynolds number in the ranges $\text{Re} < 10^4$ and $\text{Re} > 2 \times 10^5$, and a slight decrease within $2 \times 10^4 < \text{Re} < 10^5$. In particular, an increase of 63% of the mean lift slope at $\alpha = 0°$ was reported when the Reynolds number increases from 6×10^3 to 6×10^4.

Figure 12 depicts the mean and the standard deviation of the experimental pressure coefficient obtained at 2° of incidence for three Reynolds numbers. The main variation with the Reynolds number lies in the pressure magnitude: the mean suction is slightly larger on the upper surface and lower on the first and last third of the lower surface (Fig. 12a). Moreover, larger fluctuations, i.e., larger C_p', are observed at higher Reynolds number (Figs. 12b and 12c). However, the general shape of both the

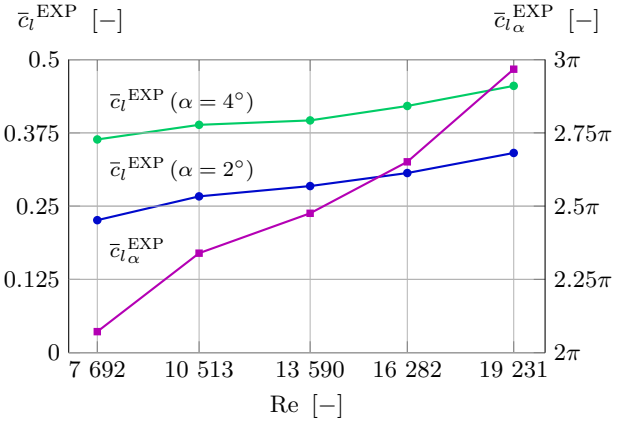

Figure 11: Mean lift coefficient and its slope depending on Reynolds number.

mean and standard deviation does not change with the Reynolds number. In particular, the location of the maximum and minimum $\overline{C}_p{}^{\mathrm{EXP}}$ and $C'_p{}^{\mathrm{EXP}}$ remains constant. Finally, the mean pressure recovery appears to begin at the same chordwise location $\overline{r}$.

The changes in the magnitude of the pressure distribution, and thus the higher lift, could possibly originate in the vertical displacement of the vortex cores. This could also be linked to an increase/decrease of the vortex strength and/or thickness. Conversely, the Reynolds number does not impact the chordwise location of the two vortices as the locations of the pressure recovery along the upper and lower surfaces are constant. Moreover, using the correlation of the reattachment point with the maximum $\overline{C}_p$, these results indicate that the reattachment point on the lower surface does not move when the Reynolds number is increased, which is also supported by the location of the maximum of C'_p not being modified by Re. These results are in contradiction to the mechanism proposed by Schewe (2013) who suggested that the modification in the turbulence level associated with a change of the Reynolds number induces a modification of the flow structure along the lower surface of the rectangle. More precisely, Schewe (2013) argued that an increase of the Reynolds number should result in a reattachment point located further upstream. The shape and curvature of the mean vortex A_L located on the lower side of the rectangular cylinder would thus be modified. The subsequent change in the mean pressure distribution would cause an increase of the mean lift. The present results are not consistent with the mechanism proposed by Schewe (2013) but rather suggest that the lift increase is related to a vertical displacement of the vortex core and/or an increase in the vortex strength/thickness.

4. Conclusions

The flow around a 4:1 rectangular cylinder at several angles of attack has been studied numerically and experimentally. In particular, dynamic pressure measurements have been performed to obtain the time response of the pressure coefficient C_p along a cross-section of the cylinder. The pressure distribution was used to compute and study the aerodynamic loads

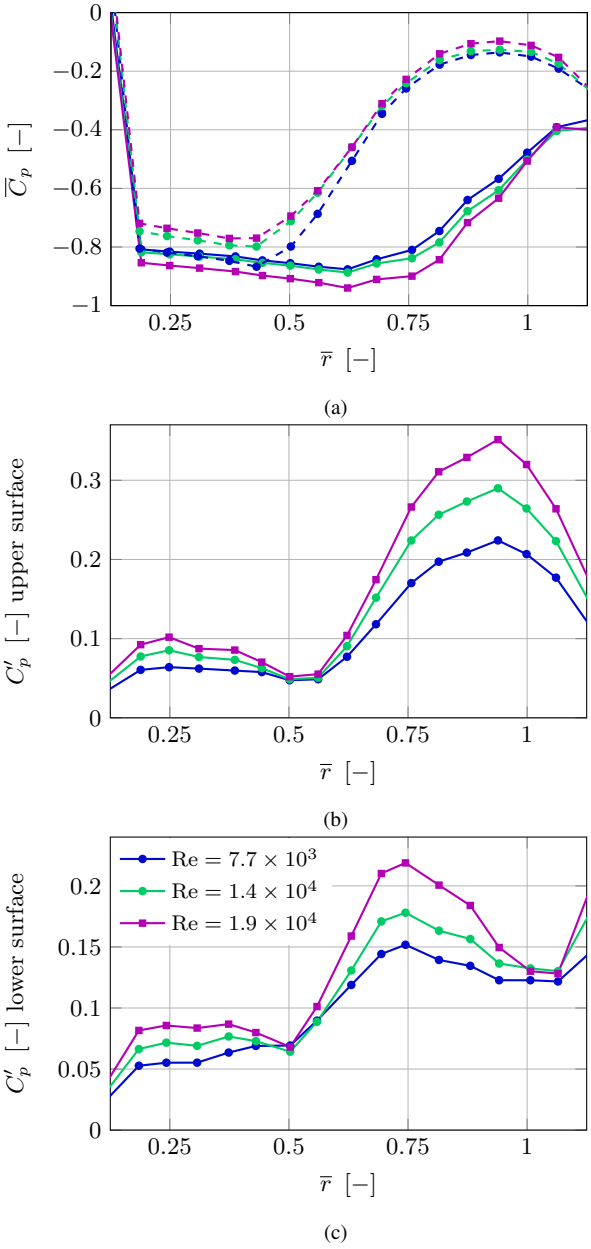

Figure 12: Mean and standard deviation of $C_p{}^{\mathrm{EXP}}$ at $\alpha = 2°$ depending on Reynolds number.

on the body and to analyze the flow dynamics. The sensitivity of the solution on the Reynolds number has been quantified by considering different Reynolds numbers ranging between 7.8×10^3 and 1.9×10^4. Additionally, URANS simulations based on the $k - \omega$ SST turbulence model and DDES simulations based on the Spalart-Allmaras model have been performed. The pressure distribution along the cross-section of the cylinder resulting from numerical computations has been compared to the experimental results through statistical analysis and a modal decomposition method, namely DMD. Moreover, numerical results have been used to visualize key flow structures.

Large discrepancies between numerical and experimental results have been highlighted. In particular, the mean suction in-

tensity along the upper surface is largely overestimated by both URANS and DDES for all the incidence angles considered. This results in an overestimation of the lift coefficient for non-zero angles of attack. Conversely, the drag coefficient is captured with satisfying accuracy by both URANS and DDES. The high sensitivity of the pressure on the flow structures explains the rather poor numerical results. Although DDES should provide a more accurate representation of turbulence, URANS has been found to perform better for incidences below the stall angle. In particular, URANS gives a better approximation of the experimental pressure coefficient distribution, both in terms of statistics and time response. However, the stall angle is correctly estimated by DDES but not by URANS. More precisely, the decrease in suction intensity along the upper surface appearing for $\alpha > 4°$ is only captured by DDES. Nonetheless, the reattaching flow along the lower surface is better approximated by URANS, also for incidences higher than the stall angle.

The DMD filtering that has been applied to the numerical and experimental spatio-temporal pressure coefficient has demonstrated that URANS is able to correctly approximate the dynamics of pressure at the wall for incidence angles lower than 4°. The analysis of the URANS results has subsequently enabled the description of the flow dynamics. In particular, at $\alpha = 0°$, it has been shown that vortices emerge and grow both at the leading and trailing edges. The leading edge vortex is convected downstream where it merges with the vortex that has grown at the trailing edge. The resulting vortex is then shed into the wake. For incidence angles $0° < \alpha \leq 4°$, the flow dynamics along the lower surface is similar. However, along the upper surface, the vortex generated at the leading edge is convected and shed into the wake without merging with the trailing edge vortex that is dissipated.

Finally, similarly to what was reported by Schewe (2013), a Reynolds number increase from 7.8×10^3 to 1.9×10^4 has been shown to impact the mean lift slope $\bar{c}_{l_\alpha}$ that strongly increases. The pressure measurements have demonstrated that an increase in Reynolds number causes an increase/decrease of the suction along the upper/lower surfaces, respectively. This results in an increase of the mean lift coefficient. Unlike the mechanism proposed by Schewe (2013), the present results suggest that this increase is not due to an expansion of the mean recirculation bubble lying along the lower surface. It is argued that the modification in the mean pressure and the resulting variation of the mean lift slope are rather due to a modification of the mean vortex strength, thickness and/or distance of its core from the surface.

Acknowledgement

Computational resources have been provided by the Consortium des Équipements de Calcul Intensif (CCI), funded by the Fonds de la Recherche Scientifique de Belgique (F.R.S.-FNRS) under Grant No. 2.5020.11.

References

Bartoli, G., Bruno, L., Buresti, G., Ricciardelli, F., Salvetti, M., Zasso, A., 2008. BARC overview document.

Bergh, H., Tijdeman, H., 1965. Theoretical and experimental results for the dynamic response of pressure measuring systems. Technical Report. Nationaal Lucht-en Ruimtevaartlaboratorium.

Bruno, L., Fransos, D., Coste, N., Bosco, A., 2010. 3D flow around a rectangular cylinder: A computational study. Journal of Wind Engineering and Industrial Aerodynamics 98, 263–276.

Bruno, L., Salvetti, M.V., Ricciardelli, F., 2014. Benchmark on the aerodynamics of a rectangular 5:1 cylinder: An overview after the first four years of activity. Journal of Wind Engineering and Industrial Aerodynamics 126, 87–106.

Carassale, L., Freda, A., Marr-Brunenghi, M., 2014. Experimental investigation on the aerodynamic behavior of square cylinders with rounded corners. Journal of Fluids and Structures 44, 195–204.

Guissart, A., 2017. Numerical and experimental study of bluff body aerodynamics. Ph.D. thesis. Université de Liège.

Mannini, C., Marra, A.M., Pigolotti, L., Bartoli, G., 2017. The effects of free-stream turbulence and angle of attack on the aerodynamics of a cylinder with rectangular 5:1 cross section. Journal of Wind Engineering and Industrial Aerodynamics 161, 42–58.

Mannini, C., Šoda, A., Schewe, G., 2011. Numerical investigation on the three-dimensional unsteady flow past a 5:1 rectangular cylinder. Journal of Wind Engineering and Industrial Aerodynamics 99, 469–482.

Menter, F., Esch, T., 2001. Elements of industrial heat transfer predictions, in: 16th Brazilian Congress of Mechanical Engineering (COBEM), pp. 26–30.

Menter, F.R., Kuntz, M., Langtry, R., 2003. Ten years of industrial experience with the SST turbulence model. Turbulence, heat and mass transfer 4, 625–632.

Mizota, T. & Okajima, A., 1981. Experimental studies of unsteady flows around rectangular prisms, in: Proceedings of the Japan Society of Civil Engineers, pp. 49–57.

Nakaguchi, H., Hashimoto, K., Muto, S., 1968. An experimental study on aerodynamic drag of rectangular cylinders. The Journal of the Japan Society of Aeronautical Engineering 16, 1–5.

Nakamura, Y., Mizota, T., 1975. Torsional flutter of rectangular prisms. Journal of Engineering Mechanics 101.

Okajima, A., 1983. Flow around a rectangular cylinder with a section of various width/height ratios. Wind Engineers, JAWE 1983, 1–19.

Patruno, L., Ricci, M., de Miranda, S., Ubertini, F., 2016. Numerical simulation of a 5:1 rectangular cylinder at non-null angles of attack. Journal of Wind Engineering and Industrial Aerodynamics 151, 146–157.

Robertson, J.M., Cermak, J.E., Nayak, S.K., 1975. A Reynolds-number effect in flow past prismatic bodies. Mechanics Research Communications 2, 279–282.

Robertson, J.M., Wedding, J.B., Peterka, J.A., Cermak, J.E., 1978. Wall pressures of separation-reattachment flow on a square prism in uniform flow. Journal of Wind Engineering and Industrial Aerodynamics 2, 345–359.

Schewe, G., 2013. Reynolds-number-effects in flow around a rectangular cylinder with aspect ratio 1:5. Journal of Fluids and Structures 39, 15–26.

Schmid, P.J., 2010. Dynamic mode decomposition of numerical and experimental data. Journal of Fluid Mechanics 656, 5–28.

Shimada, K., Ishihara, T., 2002. Application of a modified $k - \varepsilon$ model to the prediction of aerodynamic characteristics of rectangular cross-section cylinders. Journal of fluids and structures 16, 465–485.

Spalart, P.R., Jou, W.H., Strelets, M., Allmaras, S.R., others, 1997. Comments on the feasibility of LES for wings, and on a hybrid RANS/LES approach. Advances in DNS/LES 1, 4–8.

Spalart, P.R., Streett, C., 2001. Young-Person' s Guide to Detached-Eddy Simulation Grids. Technical Report. National Aeronautics and Space Administration, Langley Research Center.

Stokes, A.N., Welsh, M.C., 1986. Flow-resonant sound interaction in a duct containing a plate, II: Square leading edge. Journal of Sound and Vibration 104, 55–73.

Tamura, T., Itoh, Y., Kuwahara, K., 1993. Computational separated-reattaching flows around a rectangular cylinder. Journal of Wind Engineering and Industrial Aerodynamics 50, 9–18.

Tamura, T., Miyagi, T., Kitagishi, T., 1998. Numerical prediction of unsteady pressures on a square cylinder with various corner shapes. Journal of Wind Engineering and Industrial Aerodynamics 74-76, 531–542.

941 Wang, X., Gu, M., 2015. Experimental investigation of Reynolds number ef-
942 fects on 2d rectangular prisms with various side ratios and rounded corners.
943 Wind and Structures, An International Journal 21, 183–202.
944 Washizu, K., Ohya, A., Otsuki, Y., Fujii, K., 1978. Aeroelastic instability of
945 rectangular cylinders in a heaving mode. Journal of Sound and Vibration 59,
946 195–210.
947 Yu, D., Kareem, A., 1998. Parametric study of flow around rectangular prisms
948 using LES. Journal of Wind Engineering and Industrial Aerodynamics 77-
949 78, 653–662.